

Assessing Cross-Equivalency in Terms of Part Structure on Different L-PBF Systems

Mikyle Paul^{1,2}, Erfan Maleki^{1,2}, Shuai Shao^{1,2}, Nima Shamsaei^{1,2*}

¹ *Department of Mechanical Engineering, Auburn University, Auburn, AL 36849, USA*

² *National Centre for Additive Manufacturing Excellence (NCAME), Auburn University, Auburn,
AL 36849, USA*

* Corresponding Author:

Email: shamsaei@auburn.edu

Tel: (334) 844 4839

Abstract

Metal additive manufacturing (AM) is a manufacturing technique that continues to expand into various industries. As the development of new machines from a wide array of original equipment manufacturers (OEMs) becomes more active, so does the variability in the quality of parts produced. Equivalency in AM is an important topic which addresses this variability. Significant efforts have been made by OEMs to produce parts with consistent properties, however, this becomes challenging when trying to fabricate similar parts on systems designed by different OEMs. This is particularly important for “point-of-need” applications where there is a low tolerance for unexpected variations in properties. This study therefore aims to assess cross-equivalency between two laser powder bed fusion systems from different OEMs in terms of micro/-defect-structure and surface quality. The results showed significant differences in porosity and surface quality however, microstructure was not significantly affected.

Keywords: Laser powder bed fusion (L-PBF/LB-PBF), Ti-6Al-4V, Equivalency, Microstructure, Process induced volumetric defects

Introduction

Additive manufacturing (AM) is a manufacturing process that creates a three-dimensional object by adding material in a layer-wise manner [1–5]. Laser powder bed fusion (L-PBF) is a metal AM process that has gained popularity in various industries such as aerospace, automotive, and biomedical due to its ability to produce complex, consolidated components with good feature resolution [6–8]. However, parts fabricated using L-PBF are prone to having complex microstructures, residual stresses, and process induced volumetric defects which can negatively affect dimensional accuracy, mechanical performance, and reliability [9–14]. Laser powder bed fusion machines are designed by original equipment manufacturers (OEMs) to maintain a consistent melt pool that will result in consistent material properties throughout the fabrication process. However, due to the numerous process variables that are controlled by the machine during fabrication, even small variations in any or all of them may amount to notable differences in part quality. Controlling these variables and obtaining consistent material properties across different builds remains challenging which restricts further adoption and acceptance of L-PBF for industrial applications.

Several L-PBF OEMs exist today with each of them striving to reliably produce parts with consistent material properties. Standardization organizations have been working to produce specific standards to assist in achieving this for different L-PBF materials. However, due to the different “black boxes” on machines from different OEMs that control specific machine parameters, variations in part quality may still exist [15]. In this context, machine-to-machine equivalency in AM has been gaining attention as it aims to determine the differences in quality and performance among parts induced by different machines [16]. One of the sectors of machine-to-machine equivalency is cross-equivalency wherein the production of parts on machines from different OEMs is assessed.

Several factors such as control systems, laser type and quantity, process parameters, feedstock, recoating system, and gas flow characteristics, among others, may be different for machines from different OEMs [17]. Consequently, fabricating a part with the similar micro-/defect-structures and in turn, the same mechanical properties on different L-PBF systems may be challenging. Cross equivalency among two or more machines can be achieved by developing specific process parameters on each machine that result in similar micro-/defect-structures, which, in turn, ensures consistent mechanical performance of a component. This exercise becomes imperative for “point-of-need” applications where known material properties are essential. As a first step in assessing cross-equivalency, this study aims to investigate the differences in micro-/defect-structure and surface quality of identical parts produced by two L-PBF systems from different OEMs. Ti-6Al-4V has been used in this study due to its high demand in various industrial sectors.

Experimental procedure

Two builds consisting of nominally identical artifacts were conducted on two L-PBF systems from different OEMs including an EOS M290 and a Renishaw RenAM500Q Flex denoted as Machine 1 and Machine 2, respectively. Ti-6Al-4V grade 5 powder supplied by AP&C with a particle size distribution of 15 – 53 μm was used for fabrication on both machines to eliminate the effect of feedstock on part quality. Both machines made use of standard OEM recommended process parameters during fabrication which are presented in Table 1.

Table 1: OEM recommended Ti-6Al-4V process parameters used on both machines.

Process Parameter	Machine 1 (EOS M290)	Machine 2 (RenAM500Q)
Laser power (W)	280	170
Scanning speed (mm/s)	1200	1070
Hatch distance (μm)	140	65
Volumetric energy density (J/mm^3)	55.55	81.48
Laser spot size (μm)	100	80
Layer thickness (μm)	30	30
Layer rotation ($^\circ$)	67	67
Scan strategy	Stripe (5 mm)	Meander
Number of lasers	1	4
Laser assignment	N/A	One laser per part
Shielding gas	Argon	Argon

The build layouts used on each machine can be observed in Figure 1. Notably, Machine 1 and Machine 2 have different gas flow and recoating directions therefore, some of the test artifacts have been reorganized to take this into consideration. Direction designations following the geographical convention have been assigned to both machines with north on the far side of the build chamber, and south on the near side by the chamber door. After fabrication, the build plates were cleaned in an ultrasonic bath to remove residual powder particles from the surfaces of the artifacts. The clean build plates were then stress relieved at 704 $^\circ\text{C}$ for 1 hour in an argon atmosphere and cooled to room temperature within the furnace. Test artifacts were removed from the build plates using a wire electrical discharge machine.

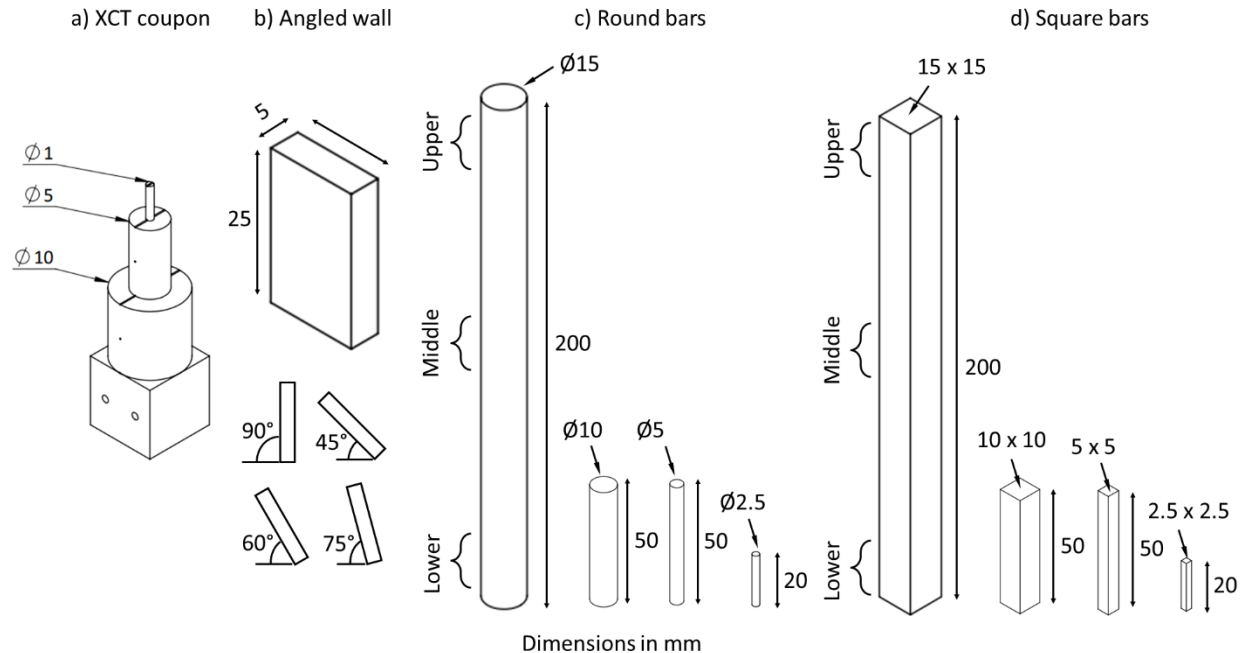


Figure 2: Test artifacts including a) XCT coupon, b) angled walls, c) round bars of various sizes, and d) square bars of various sizes.

X-ray computed tomography scans on all XCT coupons were conducted on a Zeiss Xradia 620 Versa system utilizing a source voltage of 140 kV, power of 21 W, and voxel size of 5.5 μm . The scanned volume included a cylinder 5 mm in diameter and 5 mm in height (approximately 98 mm^3). All scanned data was reconstructed using Zeiss software and the resulting image slice analysis were conducted using ImageJ and Dragonfly Pro software to obtain defect statistics. The microstructure of the material from each machine was analyzed on the 5 mm round bar on the plane perpendicular to the build direction. A small disc was cut from each bar and mounted in epoxy exposing the plane of interest. The mount was then ground until planar using 280 grit sandpaper on a semi-automatic polisher. Thereafter, polishing was conducted using an UltraPad with a 9 μm diamond suspension followed by a ChemoMet pad and 0.05 μm colloidal silica until a mirror finish was obtained. The samples were then etched using Kroll's reagent for approximately 20 seconds. Micrographs of the etched samples were obtained using a Keyence VHX-6000 optical microscope. Additionally, all R_a and S_a measurements were performed on the same optical microscope. For R_a , three 5.5 mm long lines were measured and averaged, whereas for S_a , three 4 mm^2 areas were measured and averaged.

Results and discussions

The porosity results from XCT scans on the 5 mm diameter sections of XCT coupons have been included in Figure 3 for each machine. The colored specks (green and red) represent volumetric defects within the scanned volume as viewed from the top of the coupon. Each coupon was located in a different sector on the build plate as shown in Figure 2 and oriented in the vertical direction, i.e., long axis parallel to the build direction. Two additional coupons per machine were fabricated in the horizontal (long axis perpendicular to the build direction) and diagonal (long axis inclined at 45° to the build direction) orientations (denoted as H and D, respectively) to assess the orientation effect on porosity. The defect statistics for coupons from each machine in different locations have been included in Table 2. A higher number of defects can be observed in Machine 1 as shown by the count within a 98 mm³ scan volume in Table 2. A higher concentration of defects has been observed near the surface of Machine 1 coupons compared to Machine 2 coupons. Consequently, the relative density of Machine 1 coupons is lower than Machine 2 coupons. Based on the defect statistics provided in Table 2, larger defects can be observed in Machine 1 coupons in most locations as indicated by the higher 90th percentile maximum Feret diameter.

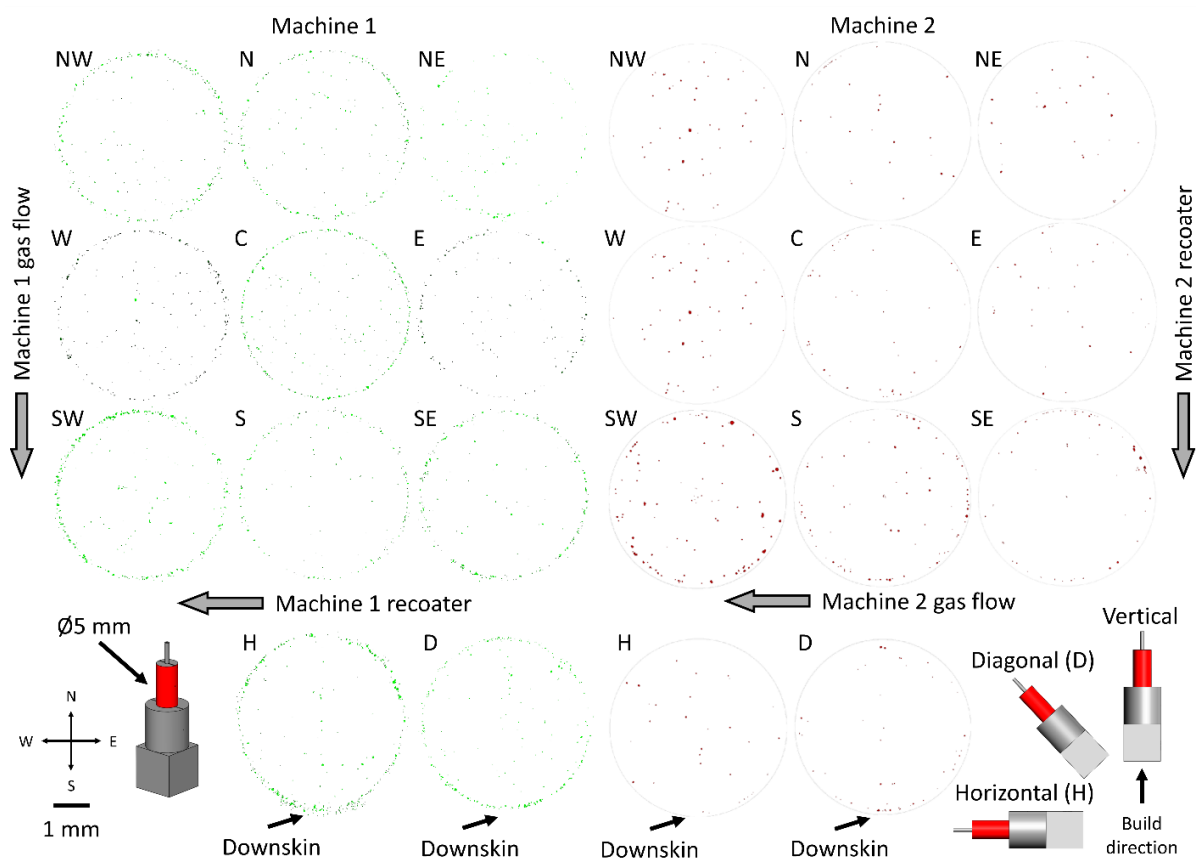


Figure 3: XCT results for both machines in the vertical orientation at different locations on the build plate (top three rows) and in horizontal and diagonal orientations (bottom row).

Table 2: Process induced volumetric defect statistics for XCT coupons from both machines at different locations on the build plate and in different build orientations. The total scanned volume is 98 mm³ per coupon.

Location/ Orientation	Machine	Max. Feret dia. (μm)	90 th percentile Max. Feret dia. (μm)	Max. equivalent sphere dia. (μm)	Relative density, ρ_{rel} , (%)	Count	Average sphericity
NW	1	105.77	60.47	57.68	99.9971	250	0.876
	2	91.77	47.21	61.53	99.9984	119	0.953
N	1	102.16	59.65	61.00	99.9971	227	0.877
	2	169.99	41.64	49.66	99.9994	61	0.962
NE	1	116.88	58.44	59.00	99.9988	113	0.848
	2	81.93	57.37	54.99	99.9994	32	0.956
W	1	209.96	58.39	83.39	99.9971	212	0.883
	2	78.21	42.46	66.91	99.9989	53	0.975
C	1	86.76	59.31	62.94	99.9956	340	0.887
	2	82.13	46.14	41.37	99.9995	53	0.959
E	1	201.12	60.45	65.57	99.9978	166	0.893
	2	53.43	40.97	44.75	99.9996	38	0.978
SW	1	101.03	68.69	64.57	99.9950	357	0.871
	2	127.45	60.94	92.40	99.9955	119	0.961
S	1	81.42	54.00	52.22	99.9981	183	0.880
	2	68.77	58.54	58.54	99.9983	107	0.954
SE	1	118.81	67.31	61.07	99.9973	235	0.865
	2	95.93	42.38	62.14	99.9990	141	0.937
D	1	113.26	58.39	68.40	99.9971	262	0.861
	2	54.80	43.68	56.17	99.9993	68	0.968
H	1	141.98	68.03	80.96	99.9939	430	0.963
	2	123.19	42.87	48.57	99.9995	41	0.963

Less defects can be observed within the interior of the coupons in Machine 1 compared to the near surface ones. Two contributing factors may result in increased near surface defects in Machine 1. Firstly, the contour process parameter on Machine 1 consists of an inner and outer contour. If there is insufficient overlap between both contours or fluctuation in laser power, defects may form at the overlapping region between the contours forming lack of fusion (LoF) defects. Secondly, overlapping regions between the infill and first contour may result in slight overheating forming keyhole (KH) defects. Machine 2, however, uses a single contour; therefore, the risk of defect formation between overlaps is reduced, however, not eliminated. Despite using a single contour, KH defects in the south region of Machine 2 can be observed which will be discussed below.

Defect population can also be observed to vary across the build plate in each machine depending on the relative location to gas flow and recoating direction. Based on the images shown in Figure 3 and the data in Table 2, the SW location shows the highest level of porosity among all other locations. This can be due to its proximity to the gas flow and recoating direction. On both machines, the SW location is the furthest away from the gas inlet and powder dispenser. The flow of gas becomes more turbulent further away from the gas inlet which reduces the overall efficiency of spatter extraction resulting in LoF defects and reduces both the thermal stability of the melt pool and heat extraction resulting in KH defects [18]. Additionally, the further away a part is from the dispenser, the more likely it is for spatter particles to be deposited on the part by the recoater as the recoater may drag spatter particles from the near side to the far side of its path [19]. The relative densities of all coupons from both machines have been separated by location and have been included in Figure 4a). Considering gas flow and recoating direction, the locations of Machine 2 have been reorganized as shown in Figure 4b) and have been noted as equivalent locations with respect to Machine 1. For instance, based on gas flow and recoating directions, NW on Machine 1 is the equivalent of SE in Machine 2. This enabled a more accurate comparison of porosity among each machine.



Figure 4: Relative density comparison of XCT coupons on different machines by location in a) along with diagonal and horizontal orientations in the last two columns. Equivalent locations considering gas flow and recoating directions are included in b). Relative density comparison based on equivalent location is provided in c).

The effects of part orientation have also been captured by fabricating diagonal and horizontal XCT coupons. The XCT results can be observed at the bottom of Figure 3. For the horizontal orientation, Machine 1 coupons show a high concentration of defects near the downskin surfaces in addition to general near surface defects around the circumference of the coupon. Although support structures were used during fabrication, downward facing surfaces may still be susceptible to an increased likelihood of defect formation at the points of the coupon that attach to the support structure. For unsupported overhanging areas or downskin surfaces, melt pools may be unstable due to lack of solid material underneath them resulting in the formation of defects. Separate process parameters are often assigned to downskin areas to combat this, however, it may still be challenging for OEMs to develop a single set of downskin process parameter that can cover a wide range of overhanging geometries. Additionally, the coupon experienced some geometric distortion. However, in the case of the Machine 2 horizontal coupon, porosity did not appear to be much more different than the vertical coupons hinting at more optimized downskin process parameters for Machine 2. Diagonal coupons were comparable with the vertical ones on both machines in terms of relative density however, slight concentrations of defects near the downward facing side of the coupons have been observed.

The surface texture of XCT coupons were also measured in terms of line arithmetic mean roughness, R_a . In Figure 5, the red section shows the portion of the XCT coupons that were used for measuring R_a , i.e., the 5 mm diameter section, and the yellow line indicates where the line profile was taken for the coupons on each machine. In the case of diagonal coupons, the downward facing surface was measured. The schematic shown in Figure 5 illustrates the section used for measurement along with a height map showing the surface texture of the scanned region for selected locations including C, NE, and SW. From the scatter plot shown in Figure 5, R_a for Machine 1 is greater than Machine 2 for all equivalent locations. However, there is no clear correlation between location and R_a . The difference in R_a between both machines may be due to the different laser spot sizes used. Machine 1 utilizes a laser spot size of 100 μm whereas Machine 2 utilizes 80 μm . A smaller spot size enables a finer resolution during fabrication improving the accuracy of the final geometry [20]. Additionally, the use of double contours on Machine 1 may also increase the likelihood of residual powder particles attaching to the part surface due to increased energy input [21].

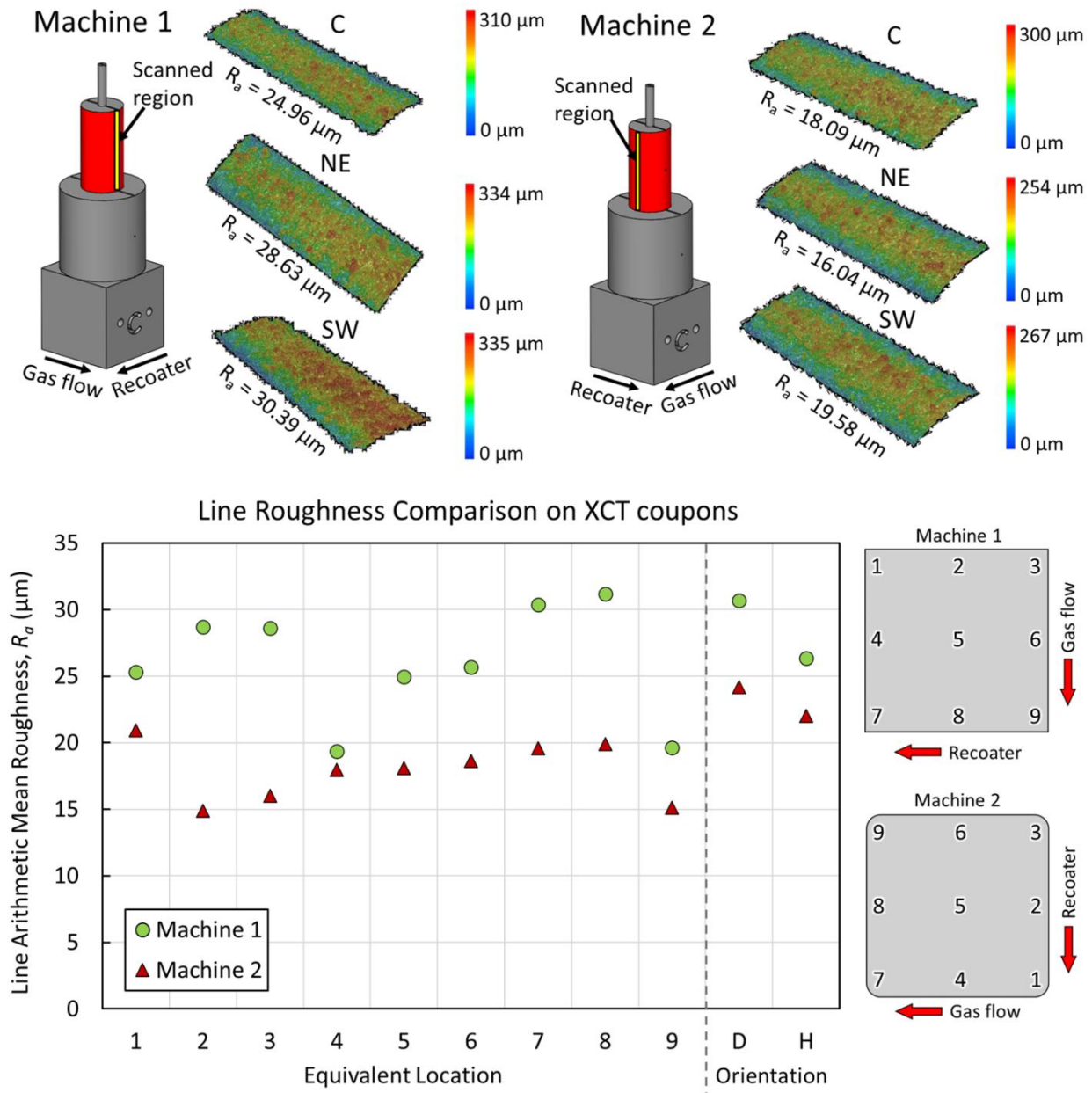


Figure 5: Line roughness comparison on XCT coupons for both machines at equivalent locations.

The size and shape effect on roughness was also considered with the use of round and square bars of different sizes (Figure 6). The surfaces facing away from the gas flow direction were selected for R_a measurements. From Figure 6a), it can be observed that there is no significant effect of size or shape on R_a , however, the separation between Machine 1 and Machine 2 can still be observed. Some separation between the data points of Machine 1 round bars can be due to variations in the sites chosen for measurement as the bars did not show any specific trend with respect to size. The opposite can be observed for the square bars on Machine 1. In general, since the surfaces of Machine 1 were not as uniform as Machine 2, variations in the measurements are

to be expected. Machine 2 measurements are quite consistent and agree with the measurements taken on the XCT coupons. The bars for Machine 2 visually appeared more uniform and felt smoother by touch as well. The effect of height on R_a was considered by separating the 15 mm thick bars into three sections as shown in Figure 6b). Machine 1 R_a measurements tend to be higher than Machine 2 as previously observed. However, no clear trend between R_a and height can be observed. The values tend to overlap with the ones observed in Figure 6a) confirming consistency in surface texture regardless of build height.

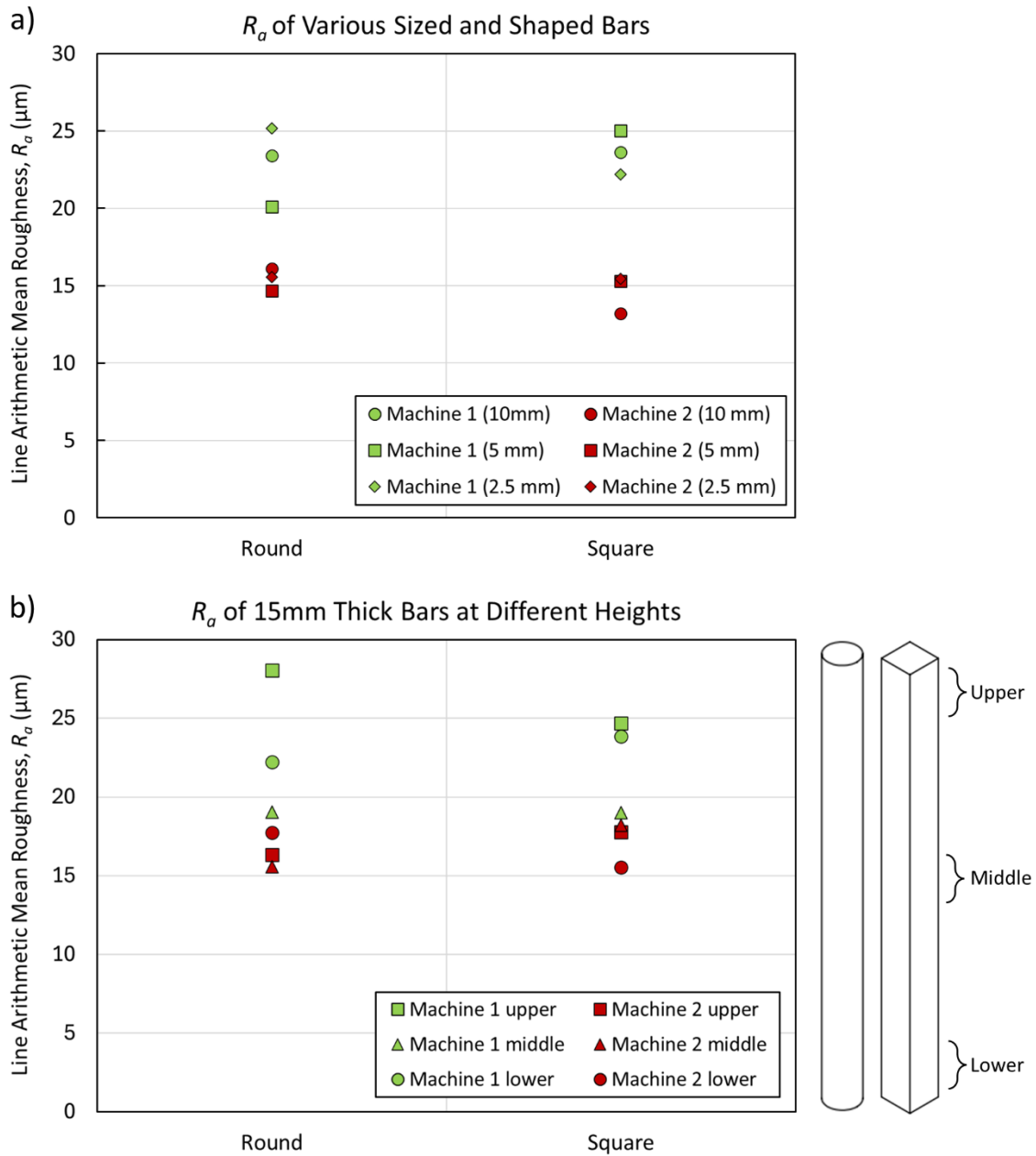


Figure 6: Line roughness measurements of a) differently sized and shaped bars, and b) 15 mm thick bars at different heights for both machines.

Surface texture in terms of surface arithmetic mean roughness, S_a , has been measured on the downward facing surfaces of angled walls. As expected, S_a can be observed to be higher for walls with a smaller angle. During fabrication of inclined surfaces, the staircase effect can be encountered. This effect can be exacerbated by thicker layers and shallower inclination angles with respect to the build plate. Shallower inclination angles result in more overhanging or unsupported material during fabrication which can reduce the stability of the melt pool and affect cooling rates. This may cause surrounding powders to adhere to the downward facing or unsupported surfaces increasing the surface roughness. As the inclination angle increases, this effect can be reduced. Machine 2 walls can be observed to have lower S_a than Machine 1. This can be due to a combination of factors including better optimization of downskin parameters on Machine 2 and the use of a smaller laser spot size which can lead to better feature resolution. A narrower spot size could lead to a less exaggerated overhanging surface due to the finer obtainable resolution.

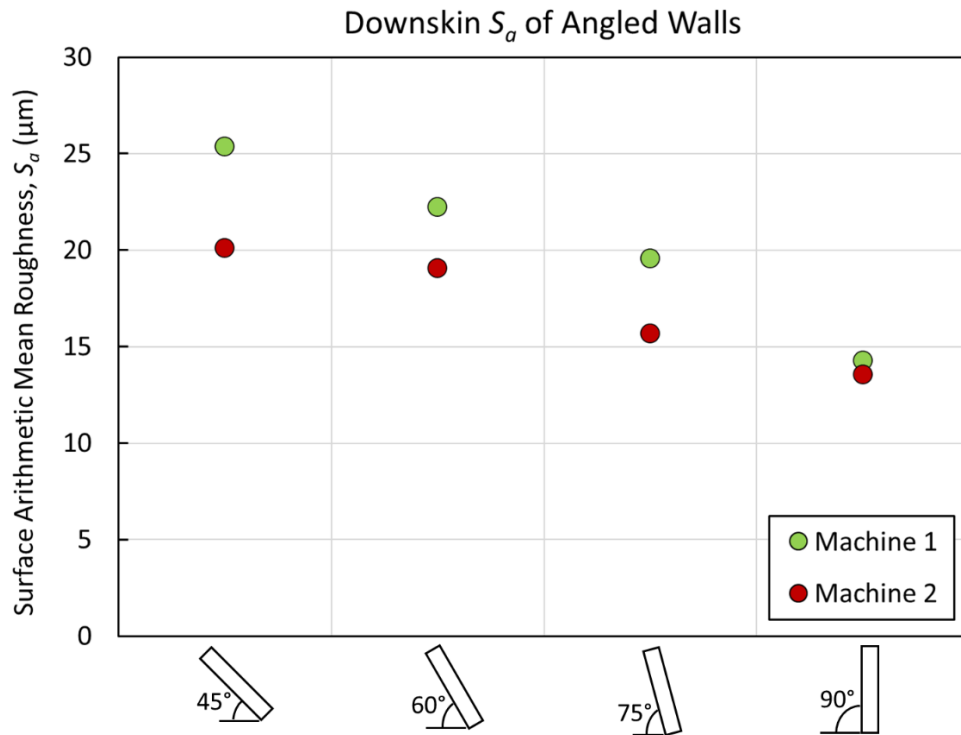


Figure 7: Downskin surface roughness of angled walls for different machines.

The microstructural results have been included in Figure 3 for each machine. The images included in Figure 3 have been obtained from an optical microscope on etched coupons. The microstructure of Machine 1 appears slightly coarser than Machine 2. The Prior β grains appear larger and thicker, respectively, for Machine 1. This could be due to the smaller spot size of the laser which results in a smaller melt pool. The differences in microstructure may result in different mechanical properties for each machine.

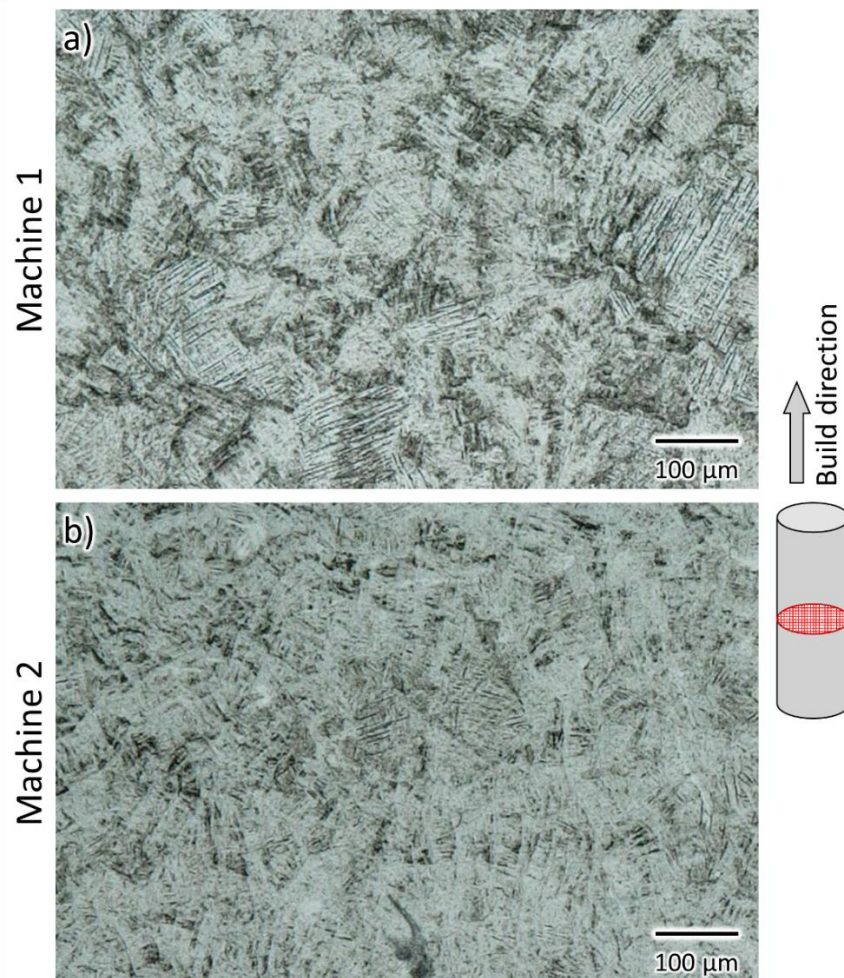


Figure 8: Microstructure of L-PBF Ti-6Al-4V fabricated on a) Machine 1 and b) Machine 2.

Conclusions

This study assessed the cross-equivalency of different L-PBF systems on Ti-6Al-4V parts. Comparisons of micro-/defect-structure and surface texture between the machines were made. The following conclusions can be drawn from the experimental results and analyses:

1. Process induced volumetric defects' population and types differed on each machine due to different volumetric energy densities and contour parameters.
2. Relative density and defect type correlated with location on the build plate with lower density and more keyhole defects were observed on coupons further away from the gas inlet and powder dispenser.
3. Finer surface texture characteristics were observed on Machine 2 artifacts likely due to the smaller laser spot size of Machine 2 resulting in higher resolution and less exaggerated staircase effect in inclined surfaces.
4. The microstructure of Machine 1 material was coarser than Machine 2 material likely due to the smaller melt pool induced by smaller laser spot size.

Acknowledgements

This research is based upon the work partially supported by the National Science Foundation (NSF) under grant No. 2319690.

References

- [1] W.E. Frazier, Metal Additive Manufacturing: A Review, *J Mater Eng Perform* 23 (2014) 1917–1928. <https://doi.org/10.1007/s11665-014-0958-z>.
- [2] N. Shamsaei, A. Yadollahi, L. Bian, S.M. Thompson, An overview of Direct Laser Deposition for additive manufacturing; Part II: Mechanical behavior, process parameter optimization and control, *Addit Manuf* 8 (2015) 12–35. <https://doi.org/10.1016/J.ADDMA.2015.07.002>.
- [3] M. Paul, R. Ghiaasiaan, P. Gradl, J. Caron, P. Wang, S. Shao, N. Shamsaei, Tensile and fatigue behaviors of newly developed HAYNES® 233 alloy: Additively manufactured vs. wrought, *Mater Des* 244 (2024) 113165. <https://doi.org/10.1016/J.MATDES.2024.113165>.
- [4] B. Blakey-Milner, P. Gradl, G. Snedden, M. Brooks, J. Pitot, E. Lopez, M. Leary, F. Berto, A. du Plessis, Metal additive manufacturing in aerospace: A review, *Mater Des* 209 (2021) 110008. <https://doi.org/10.1016/j.matdes.2021.110008>.
- [5] S. Lee, Z. Ahmadi, M. Paul, M. Mahjouri-Samani, S. Shao, N. Shamsaei, In-situ tension investigation of additively manufactured silver lines on flexible substrates, *Additive Manufacturing Letters* 7 (2023) 100171. <https://doi.org/10.1016/J.ADDLET.2023.100171>.
- [6] I. Yadroitsev, A. Du Plessis, I. Yadroitsava, Basics of laser powder bed fusion, *Fundamentals of Laser Powder Bed Fusion of Metals* (2021) 15–38. <https://doi.org/10.1016/B978-0-12-824090-8.00024-X>.
- [7] R. Singh, A. Gupta, O. Tripathi, S. Srivastava, B. Singh, A. Awasthi, S.K. Rajput, P. Sonia, P. Singhal, K.K. Saxena, Powder bed fusion process in additive manufacturing: An overview, *Mater Today Proc* 26 (2020) 3058–3070. <https://doi.org/10.1016/J.MATPR.2020.02.635>.
- [8] D. Dev Singh, T. Mahender, A. Raji Reddy, Powder bed fusion process: A brief review, *Mater Today Proc* 46 (2021) 350–355. <https://doi.org/10.1016/J.MATPR.2020.08.415>.
- [9] P.J. Wilson, E. Azizian-Farsani, M. Paul, M.M. Khonsari, S. Shao, N. Shamsaei, On the damping and fatigue characterization of additively manufactured Ti-6Al-4V, *Additive Manufacturing Letters* 11 (2024) 100260. <https://doi.org/10.1016/j.addlet.2024.100260>.
- [10] M. Paul, S. Soman, S. Shao, N. Shamsaei, Fatigue crack growth in L-PBF Ti-6Al-4V: Influence of notch orientation, stress ratio, and volumetric defects, *Int J Fatigue* 198 (2025) 109027. <https://doi.org/10.1016/J.IJFATIGUE.2025.109027>.

- [11] P. Mercelis, J.P. Kruth, Residual stresses in selective laser sintering and selective laser melting, *Rapid Prototyp J* 12 (2006) 254–265. <https://doi.org/10.1108/13552540610707013>.
- [12] H. Gong, K. Rafi, T. Starr, B. Stucker, Effect of Defects on Fatigue Tests of As-Build Ti-6Al-4V Parts Fabricated by Selective Laser Melting, (2012). <https://doi.org/10.26153/TSW/15369>.
- [13] E. Maleki, B. Salehnasab, M. Paul, S. Shao, N. Shamsaei, Dimensional accuracy of fabricated geometries through powder bed fusion: An overview and a new benchmark artifact proposal, *Mater Des* 257 (2025) 114361. <https://doi.org/10.1016/J.MATDES.2025.114361>.
- [14] I. Nandi, R. Ghiaasiaan, N. Ahmad, P.R. Gradl, N. Shamsaei, Effect of heat treatment on the microstructure and mechanical properties of Monel K500 alloy fabricated via L-PBF and LP-DED, (2023). <https://doi.org/https://doi.org/10.26153/tsw/50947>.
- [15] J.M. Costa, E.W. Sequeiros, R.F. Santos, M.F. Vieira, Benchmarking L-PBF Systems for Die Production: Powder, Dimensional, Surface, Microstructural and Mechanical Characterisation, *Metals* 2024, Vol. 14, Page 520 14 (2024) 520. <https://doi.org/10.3390/MET14050520>.
- [16] F. Uriati, G. Nicoletto, A comparison of Inconel 718 obtained with three L-PBF production systems in terms of process parameters, as-built surface quality, and fatigue performance, *Int J Fatigue* 162 (2022) 107004. <https://doi.org/10.1016/J.IJFATIGUE.2022.107004>.
- [17] M.S. Yasin, K. Stonaker, S. Shao, N. Shamsaei, Mechanical performance of laser powder bed fused Ti-6Al-4V: The influence of filter condition and part location, *Additive Manufacturing Letters* 11 (2024) 100255. <https://doi.org/10.1016/J.ADDLET.2024.100255>.
- [18] M. Costes, L. Arnaud, P. Lefebvre, Q. Mandou, Experimental study of laser powder bed fusion (L-PBF) gas shield inlet optimization and its effects on part quality, *The International Journal of Advanced Manufacturing Technology* 133 (2024) 5299–5318. <https://doi.org/10.1007/s00170-024-14035-3>.
- [19] Z. Li, H. Li, J. Yin, Y. Li, Z. Nie, X. Li, D. You, K. Guan, W. Duan, L. Cao, D. Wang, L. Ke, Y. Liu, P. Zhao, L. Wang, K. Zhu, Z. Zhang, L. Gao, L. Hao, A Review of Spatter in Laser Powder Bed Fusion Additive Manufacturing: In Situ Detection, Generation, Effects, and Countermeasures, *Micromachines* 2022, Vol. 13, Page 1366 13 (2022) 1366. <https://doi.org/10.3390/MI13081366>.
- [20] S. Qu, J. Ding, J. Fu, M. Fu, B. Zhang, X. Song, High-precision laser powder bed fusion processing of pure copper, *Addit Manuf* 48 (2021) 102417. <https://doi.org/10.1016/J.ADDMA.2021.102417>.

- [21] M. Leary, M. Khorasani, A. Sarker, J. Tran, K. Fox, D. Downing, A. Du Plessis, Surface roughness, *Fundamentals of Laser Powder Bed Fusion of Metals* (2021) 179–213. <https://doi.org/10.1016/B978-0-12-824090-8.00023-8>.